

# Chapter 19

## Numerical Simulation of Heat Transfer and Fluid Flow in Co-axial Laser Cladding of Ti6Al4V Alloys



Vijay Mandal , Shashank Sharma  and J. Ramkumar 

**Abstract** In this article, a 2D FEM model is built to simulate the heat transfer and fluid flow in the laser cladding process of the Ti6Al4V alloy. Physical phenomena such as melt pool generation, mass addition due to powder flow, Marangoni convection, and re-solidification of the melt pool have been incorporated in the developed model. The governing equations pertaining to mass, momentum, and energy were solved in a Lagrangian moving frame to predict temperature and velocity field along with geometrical dimensions of the deposited clad. The temperature and temperature gradients were calculated at “14” located points in three different directions, to scrutinize the thermal behavior of the melt pool. Further, the influence of driving forces such as Marangoni force and thermal buoyancy force was analyzed. The prediction of microstructure evolution was based on the estimation of the temperature gradient, cooling rate, and solidification rate in the fusion zone.

**Keywords** Laser cladding · Heat transfer and fluid flow · Solidification rate

### 19.1 Introduction

Titanium and its alloys have become essential for structural applications in aerospace, electronics, and bio-medical industries, due to its lightweight and high strength to weight ratio [1, 2]. The surface properties such as corrosion resistance, thermal resistance, and tribological properties profoundly affect the functionality of any component. The major drawback of Ti alloys is relatively high wear rate [3]. Enhancement

---

V. Mandal · S. Sharma (✉) · J. Ramkumar  
Department of Mechanical Engineering, Indian Institute of Technology, Kanpur 208016, India  
e-mail: [kshashan@iitk.ac.in](mailto:kshashan@iitk.ac.in)

V. Mandal  
e-mail: [vijaym@iitk.ac.in](mailto:vijaym@iitk.ac.in)

J. Ramkumar  
e-mail: [jrkumar@iitk.ac.in](mailto:jrkumar@iitk.ac.in)

© Springer Nature Singapore Pte Ltd. 2020  
M. S. Shunmugam and M. Kanthababu (eds.), *Advances in Simulation, Product Design and Development*, Lecture Notes on Multidisciplinary Industrial Engineering,  
[https://doi.org/10.1007/978-981-32-9487-5\\_19](https://doi.org/10.1007/978-981-32-9487-5_19)

of surface properties with the help of surface modification techniques such as electroplating, chemical coating, anodic oxidation process, hot dipping, thermal spraying, and vapor deposition is extensively used to overcome the drawbacks mentioned above. However, these processes pose several limitations (i.e., the additional medium is required, toxic, pyrophoric, corrosive, etc.) [4]. One such method that can alleviate the impediments offered by the aforementioned techniques is laser cladding process. Laser has the capability to accumulate high energy on a material which is temporally and spatially confined. The large thermal gradients and high cooling rates transform the grain structure rendering excellent wear-resistant surface. The direct metal deposition through laser is a process of free-form powder deposition by means of the heat source with a high thermal gradient, and the net shape of structure can be obtained directly from the metal powder [5].

Therefore, in laser cladding, continuous efforts have been put forth by the researchers all around the world to improve the various process; for instance, Peyre et al. [6] developed a thermal model which predicts morphology and thermal behavior during multi-layer laser cladding using COMSOL Multiphysics. They reported that the numerical approach is in good covenant with the experimental results such as powder temperature with radius, melt pool geometry at different processing parameters (i.e., scanning speed, laser intensity, and radius of powder delivery), and spatial temperature variation with respect to time. In a similar approach, Kong and Kovacevic [7] conducted experiments and validated with the numerical simulation data. The influence of clad geometry on the input process parameters, i.e., laser power ( $P$ ), scanning speed ( $V$ ), and the mass flow rate ( $\dot{m}$ ) was studied. They reported that clad height increases with an increase in laser power ( $P$ ) and powder  $\dot{m}$ . However, dilution decreases with an increase in  $V$  and powder feed rate. Bedenko et al. [8] investigate an experimental and theoretical model in the laser cladding process. They reported that characteristic size of the bead (i.e., height ( $H$ ) and width ( $W$ ) of clad) decreases with increase in  $V$ , however, increases with an increase in  $P$  and  $\dot{m}$ . The scanning speed ( $V$ ) plays a vital role in fluid flow in the melt pool. At higher  $V$ , due to less interaction time, Marangoni convection is less significant, and the powder particles impinging the melt pool surfaces govern the fluid flow at this stage. However, at low scanning speed, fluid convection due to Marangoni effect is dominant. Kumar and Roy [9] scrutinized the effect of Marangoni convection on microstructural evolution. They reported finer microstructures at the bottom of the clad parts for a positive value of Marangoni number ( $Ma$ ), whereas for a negative value of  $Ma$ , the finer microstructures were observed at the top surface of the melt pool. They also noted that the influence of microstructure does not largely depend on  $V$ . Moreover, the microstructure plays a vital role in the surface properties of the clad part. For instance, Gan et al. [10] simulated the heat transfer, fluid flow, and multi-component mass transport of alloy. They predicted the solidification parameters such as solidification rate ( $R$ ), cooling rate ( $Tt$ ), and temperature gradient ( $G$ ). They reported that the temperature gradient in the periphery is higher (1352 K/mm); however, at the center of the melt pool,  $G$  was comparatively lower (650 k/mm). They also reported that the microstructure changes from planner front to equiaxed dendrite from bottom to top of the melt pool.

Therefore, to better understand the process dynamics, a simplified two-dimensional numerical model is constructed. The present study takes into account heat transfer, fluid flow, and transient powder addition on the substrate to scrutinize the levels of temperature, temperature gradients, and Marangoni convection induced velocity profiles during laser cladding. Further, the dimensional analysis was studied to comprehend the importance of heat transfer by diffusion and advection, and roles of driving forces such as Marangoni force and thermal buoyancy force. For the microstructure prediction,  $G$ ,  $Tt$ , and  $R$  have been discussed.

## 19.2 Model Implementation and Assumptions

To understand the physical process occurring in laser cladding, a 2D model considering heat transfer, melt flow dynamics along with analysis of solidification parameters such as thermal gradient and solidification rate has been formulated. In this model, there are following assumptions to be made: (1) Incompressible, laminar fluid flow in the melt region is taken into consideration. (2) The thermo-physical properties of the work materials are temperature dependent. (3) The buoyancy effect in the melt region of this model is taken into account using Boussinesq approximation. (4) The shrinkage effect during solidification is not considered in this model. (5) The vaporization effect is also not considered.

### 19.2.1 Governing Equations

Mass Conservation: The governing continuity equation is defined by

$$\frac{\partial \rho}{\partial t} + \nabla \cdot (\rho \vec{u}) = 0 \quad (19.1)$$

Energy Conservation: The governing energy conservation equation is defined by

$$\frac{\partial(\rho C_p T)}{\partial t} + \vec{u} \cdot \nabla(\rho C_p T) = \nabla \cdot (K \nabla T) \quad (19.2)$$

During the phase change, values of  $\rho$ ,  $C_p$ , and  $k$  were calculated by the following equations:

$$\rho = \theta \rho_{\text{phase 1}} + (1 - \theta) \rho_{\text{phase 2}} \quad (19.3)$$

$$C_p = \frac{1}{\rho} (\theta \rho_{\text{phase 1}} C_{p,1} + (1 - \theta) \rho_{\text{phase 2}} C_{p,2}) + L \frac{\partial \alpha_m}{\partial T} \quad (19.4)$$

$$k = \theta k_{\text{phase 1}} + (1 - \theta)k_{\text{phase 2}} \quad (19.5)$$

In Eqs. (19.3)–(19.5), phase 1 symbolizes the solid phase, i.e., solid metal, phase 2 symbolizes the liquid phase, i.e., molten metal, and  $\theta$  is a linear function, lies between 0 and 1.

Momentum Conservation: The momentum conservation equation is defined by

$$\frac{\partial(\rho\vec{u})}{\partial t} + \vec{u} \cdot \nabla(\rho\vec{u}) = -\nabla p + \nabla \cdot (\mu(\nabla\vec{u} + (\nabla\vec{u})^T)) + \vec{F}_c + \vec{F}_d \quad (19.6)$$

This equation is implemented in the entire computational domain including melted and solid metal region. For dissipating velocity field in the solid region, the viscosity in the solid region is taken to be a very high value ( $\sim 1000$ ). The source term  $\vec{F}_c$  is used in the mushy zone (or porous media). The term  $\vec{F}_d$  can be defined as

$$\vec{F}_d = -\frac{C(1 - f_l)^2}{b + f_l^3}\vec{u} \quad (19.7)$$

Here,  $\vec{F}_d$  represents the momentum sink term for the mushy zone as indicated by the Carman–Kozeny equation in porous media. The constant term “ $C$ ” represents the morphology constant, and very large value is taken, i.e.,  $2 \times 10^7$  [10]. Another constant term  $b$  represents very small, i.e.,  $10^{-5}$  to avoid the source term, and  $\vec{F}_d$  is coming to be infinity. In this equation, the term  $f_l$  represents the liquid fraction depends on solidus temperature ( $T_s$ ) and liquidus temperature ( $T_l$ ) and is defined as

$$f_l = \begin{cases} 0 & T < T_s \\ \frac{T - T_s}{T_l - T_s} & T_s < T < T_l \\ 1 & T > T_l \end{cases} \quad (19.8)$$

The source term  $\vec{F}_c$  in Eq. (19.6) is defined by

$$\vec{F}_c = \rho_{\text{liquid}}\vec{g}\beta_T(T - T_{\text{ref}}) \quad (19.9)$$

In Eq. (19.9),  $\rho_{\text{liquid}}$  is density of the liquid, and  $\beta_T$  and  $T_{\text{ref}}$  are listed in Table 19.1.

Marangoni Convection: The above equation defines the forces induced due to Marangoni convection at the interface (or free surface).

$$\mu\left(\frac{\partial u}{\partial y}\right) = -\left(\frac{\partial \gamma}{\partial T}\right)\left(\frac{\partial T}{\partial x}\right) \quad (19.10)$$

In this Eq. (19.10),  $\mu$  and  $\gamma$  represent the viscosity and surface tension, respectively.

**Table 19.1** Thermo-physical properties of Ti6Al4V

Property	Symbol	Value	Ref.
Liquidus temperature	$T_l$	1923 K	[11]
Solidus temperature	$T$	1873 K	[11]
Ambient temperature	$T_{ref}$	293.15 K	
Density	$\rho$	4420 kg/m <sup>3</sup>	
Thermal conductivity	$k$	W/mK	[12]
Specific heat capacity	$c_p$	J/(kg K)	[12]
Convection coefficient	$h$	50 W/m <sup>2</sup> K	
Emissivity	$\epsilon$	0.4	[11]
Dynamic viscosity	$\mu$	$4 \times 10^{-3}$ kg/(m s)	[11]
Absorptivity	$A$	0.4	[11]
Stefan–Boltzmann constant	$\sigma$	$5.67 \times 10^{-8}$ W/m <sup>2</sup> K <sup>4</sup>	[11]
Thermocapillary coefficient	$\partial\gamma/\partial T$	$-2.7 \times 10^{-4}$ N/mK	[11]
Thermal expansion coefficient	$\beta_T$	$2 \times 10^{-4}$ 1/K	[11]

Boundary Conditions: The time-dependent Gaussian heat source as shown in Fig. 19.1 is estimated by

$$q = \frac{2AP}{\pi R^2} e^{-\frac{x^2}{R^2}} e^{-\frac{2(vt-R)^2}{R^2}} \tag{19.11}$$

where A is absorptivity of Ti6Al4V. At top of the surface, energy balance equation is defined by

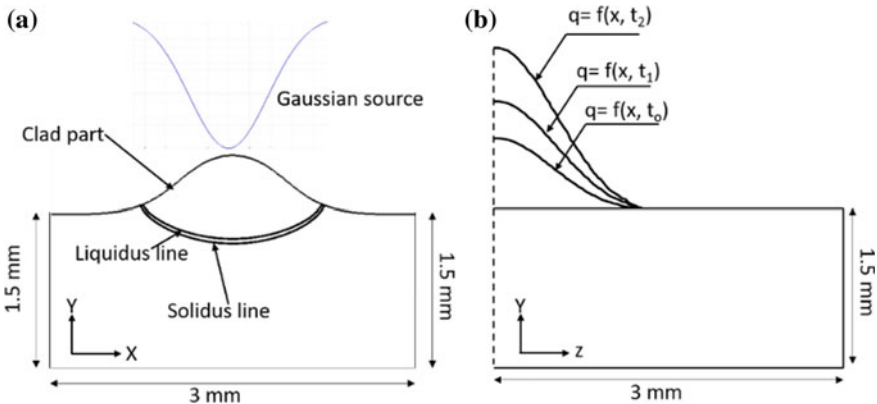


**Fig. 19.1** a Schematic diagram of the laser cladding process and b variation of laser intensity with respect to time

$$k \frac{\partial T}{\partial n} = q - h(T - T_\infty) - \varepsilon \sigma (T^4 - T_\infty^4) \quad (19.12)$$

In this Eq. (19.12), 1st, 2nd, and 3rd terms on the right-hand side are incoming heat energy, heat loss due to convection, and radiation heat loss to the ambient, respectively. In Eq. (19.12), the terms  $h$ ,  $\varepsilon$ , and  $\sigma$  are listed in Table 19.1. Force balance at the top-most surface is the following boundary conditions.

$$\left[ \mu \left( \vec{\nabla} u + \left( \vec{\nabla} u \right)^T \right) \right] \vec{n} = \sigma k \nabla \phi \vec{i} + \frac{\partial \sigma}{\partial T} \frac{\partial T}{\partial x} \vec{j} \quad (19.13)$$

Above boundary condition mainly defines the melt pool dynamics in laser cladding. The first term describes towards the effect of surface tension, i.e., minimizing energy distribution by changing the shape of its surface, whereas the second term accounts for Marangoni convection (Eq. 19.10) which is responsible for distribution of molten metal according to the distribution of temperature in the computational domain.

As for rest of three boundaries, balance heat flux at the surfaces of the following boundary equation

$$-K \nabla T = -h(T - T_{\text{ref}}) \quad (19.14)$$

No slip at the rest of the surfaces of the resulting boundary equation

$$u = 0 \quad (19.15)$$

To predict the surface profile during laser cladding process, a Lagrangian mesh is used.

Mass addition: In this model, it is assumed that the mass addition is Gaussian in nature, and also the velocity of the heat source and mass addition are same. The term  $u_p$  describes the moving velocity owing to the mass addition. It can be evaluated by the following equation:

$$u_p = \frac{\dot{m} \varepsilon_p}{\rho \pi r_p^2} \exp\left(\frac{-x^2}{r_p^2}\right) f(t) \quad (19.16)$$

In this Eq. (19.16),  $\rho$  = density of powder, and  $\dot{m}$ ,  $\varepsilon_p$ , and  $r_p$  are listed in Table 19.2. The term  $f(t)$  is defined as

$$f(t) = \begin{cases} 1 & 0 < t < 130 \text{ ms} \\ 0 & t > 130 \text{ ms} \end{cases} \quad (17)$$

**Table 19.2** Parameters used for simulation

Parameters	Symbol	Value
Laser power	$P$	400 W
Scanning speed	$V$	400 mm/min
Beam radius	$R$	0.65 mm
Mass flow rate	$\dot{m}$	1.5 g/min
Mass flow radius	$r_p$	0.65 mm
Efficiency of powder catchment	$\varepsilon_p$	0.6

### 19.2.2 Material and Parameters Used for Simulation

In this study, Ti6Al4V was used for both powder and substrate materials. The thermo-physical properties of Ti6Al4V alloys are listed in Table 19.1. Thermal conductivity and specific heat capacity are important characteristics of the materials, and these two parameters depend on the temperature [12]. The processing parameters for the study of laser cladding of Ti6Al4V are shown in Table 19.2.

## 19.3 Results and Discussion

### 19.3.1 Study of Thermal Cycle at Various Location in the Melt Pool

In Fig. 19.2a, different points (5–17) were located in the computational domain. These points are located in three different directions such as horizontal, vertical, and 45° from the horizontal. The located point “10” positions at the midpoint of the melt pool. In this model, surface deformation has been coupled with heat transfer and fluid flow. Normal Gaussian distribution velocity is acted at the top of the surface, due to this velocity, the top surface of the computational domain will move upward with time. The located points are mapped into the moving frame, that is with the direction of deformation, to capture the levels of temperature and temperature gradient with transient powder addition. The rate of deposition depends on mass flow rate and interaction time. With the increase in the value of mass flow rate and interaction time, the deposition rate increases, and it leads to an increase in the dimension of the clad part. The intensity of the laser source at the center is comparatively higher with respect to radial direction. Due to change in its intensity, the temperature at a different location in the melt pool varies. The intensity of the heat source is increased from  $t = 0$  ms to  $t = 130$  ms and then decreases from  $t = 130$  ms to  $t = 400$  ms. The variation of the temperature of all the located points periodically increases up to 130 ms, while the temperature variation exponentially decreases from 130 ms to 400 ms as shown in Fig. 19.2a. At the located point “10,” the maximum temperature

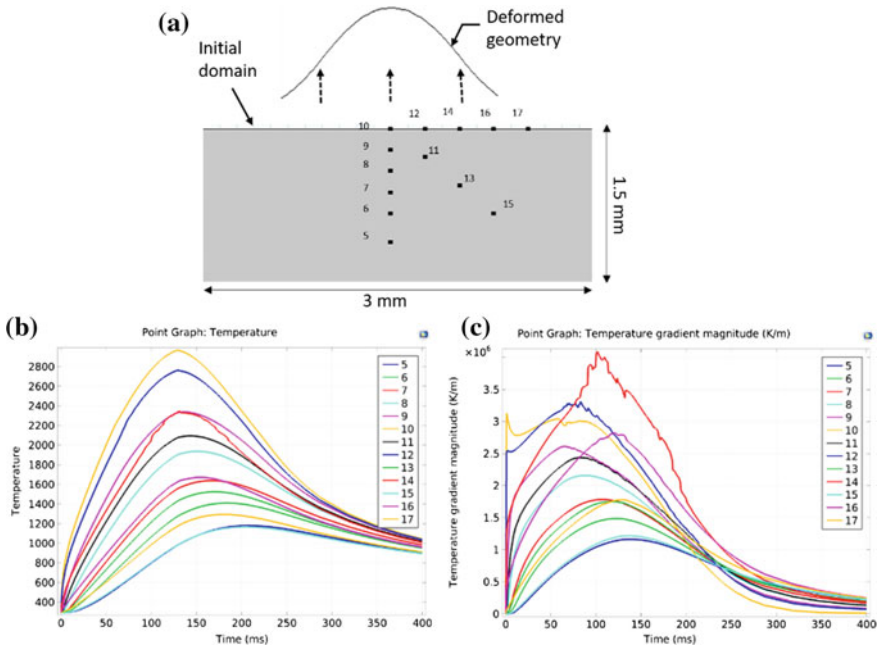


**Fig. 19.2** a Schematic diagram of computational domain depicting deformed geometry, b temperature variation with time, and c magnitude of the temperature gradient with time

was found to have a value of 2966 K which is less than the vaporization temperature [13] of Ti6Al4V alloys. However, the points “5” and “15” depict comparatively lower temperature and reach up to 890 K.

In this model, the magnitude of the temperature gradient ( $G$ ) at the located points is also predicted as shown in Fig. 19.2c. From the above figure, it can be observed that up to 38.8 ms, the maximum value of  $G$  is noticed at the point 10. However, the maximum of  $G$  was observed in the range of 38.8–77 ms, at the designated point 12. In the time period from 77 ms to 233.5 ms, the magnitude of the maximum temperature gradient was seen at the located point 14. It is pertinent to note that after reaching the maximum value of  $G$  at the located point 10, it is suddenly decreasing because of convection loss. Thus from the results, it can be concluded that the  $G$  attains their maximum value along the edge of the melt pool, due to a drastic change in temperature from its center. From the above results, it can be concluded that  $G$  varies from point to point with time. Also from the predicted model, the value of  $G$  at any located point is not the global maxima at all the time period. The aforementioned variation in  $G$  can be attributed to the presence of strong Marangoni currents present in the melt pool, discussed in later section.



### 19.3.2 Study of Heat Transfer and Hydrodynamics Fluid Flow in Clad Melt Pool

In this section, the study of temperature distribution, velocity field, and geometry of the melt pool has been demonstrated. Figure 19.3a–h represents the temperature distribution and evolution of geometry of the clad melt pool during the heating period at 30, 90, 110, and 130 ms and during the cooling period at 140, 170, 200, and 220 ms. Similarly, the velocity field distribution during heating and cooling period at different time steps as shown in Fig. 19.4a–h. Note that the laser intensity increases from 0 ms to 130 ms and decreases from 130 ms to 400 ms, according to the interaction time function discussed in Eq. (19.11) to incorporate the moving heat source condition. The spatial temperature and velocity profiles of fluid flow in the clad melt pool of cladding are indicated by color map and velocity vector arrows, respectively. The two temperature contours at the bottom are representing the solidus and liquidus

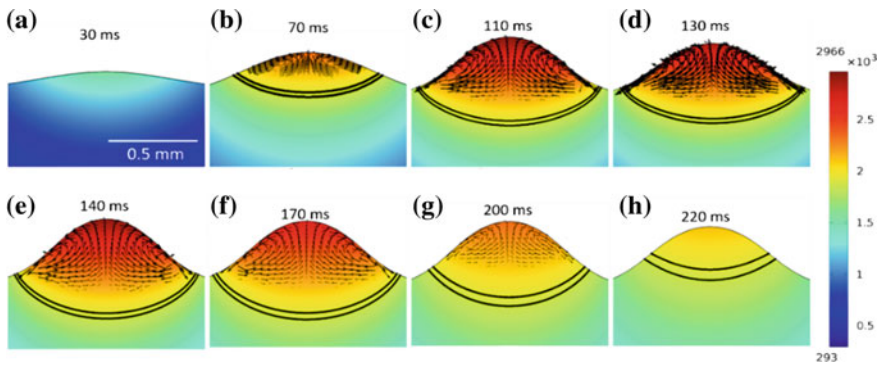


Fig. 19.3 Temperature distribution during heating a–d and cooling e–h, temperature in K

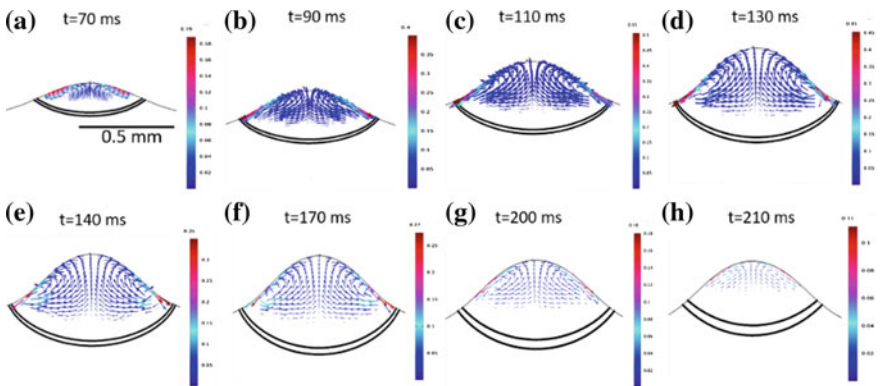


Fig. 19.4 Velocity field distribution during heating a–d and cooling e–h, velocity in (m/s)

temperature. In this figure, it can be seen that the dimension of the melt pool (i.e., width and height) continuously grows because of the addition of material and increase in temperature. The above phenomena are consistent till the intensity of laser starts to decrease at that instant the powder addition condition also ceases to act. Therefore, the melt pool and dimension of the clad increase up to 130 ms, and after 130 ms, the dimension of the clad remains constant, while the melt pool dimension decreases continuously.

The fluid flow velocity is an essential characteristic of the laser cladding process. At the initial stages of the time period the fluid flow, Marangoni convection is relatively low and flows due to the material deposition, and thermal buoyancy prevails. At later stages, after 70 ms, velocity of fluid flow is relatively higher ( $>0.4$  m/s) because of strong Marangoni convection acting at the surface of the melt pool. The maximum value of temperature in the clad melt pool was found to be 2966 K at 130 ms, while the maximum magnitude of velocity was achieved 0.51 m/s at 110 ms as shown in Fig. 19.4e. Also, observed from the above Fig. 19.4a–h, the magnitude of velocity in the clad melt pool at  $t = 110$  ms is 0.51 m/s and at  $t = 130$  ms is 0.45 m/s, while the intensity of the beam is higher at 130 ms as compared to  $t = 110$  ms because of persistent melt pool convection owing to the presence of Marangoni effects. Moreover, the melt pool velocity decreases after 130 ms because of an abrupt drop of the incoming heat flux, resulting in the decrease of  $G$ .

### 19.3.3 Analysis of the Non-dimensional Number in the Clad Melt Pool

The three non-dimensional numbers such as Marangoni number (Ma), Peclet number (Pe), and Grashof number (Gr) were analyzed to comprehend the hydrodynamics performance of fluid flow in the clad melt pool. In this model, the fluid flow in the melt pool due to thermal buoyancy and Marangoni force was considered. The Marangoni number is defined as  $Ma = \frac{\rho l_c \Delta T \left| \frac{\partial \gamma}{\partial T} \right|}{\mu^2}$  where  $l_c$  is the characteristics length,  $\Delta T$  is the difference of temperature at the center of the melt pool and solidus temperature, and  $\rho$ ,  $\frac{\partial \gamma}{\partial T}$ , and  $\mu$  are listed in Table 19.1. Moreover, the Grashof is defined as  $Gr = \frac{\rho^2 \beta g \Delta T l_d^3}{\mu^2}$  where  $g$  is termed as acceleration due to gravity, and  $l_d$  is the characteristics length (1/8th of width) of the clad melt pool. The another non-dimensional quantity is Peclet number (Pe) which is defined as  $Pe = \frac{u_m \rho c_p l_c}{k}$  where  $u_m$  is the mean velocity of the melt pool. Each of three non-dimensional numbers plays a vital role in the clad melt pool. The formulated non-dimensional number (Rf) is the ratio of Ma to Gr. The non-dimensional number Rf, having much higher value than the unity as shown in Table 19.3, leads to fluid flow in the clad melt pool mainly signifies the dominance of the Marangoni convection over the buoyancy force in the melt pool. In this model, the calculated value of non-dimensional number Pe is considerably

**Table 19.3** Magnitude value of various dimensionless number at  $t = 130$  ms

Power	Ma	Gr	Pe	Rf = Ma/Gr
400 W	40,762.068	0.5785	27	70,461.65

higher than unity, demonstrates the prominent effect of heat transfer by advection, while the heat transfer by diffusion has a minor role.

### 19.3.4 Analysis of Melt Pool Geometry

The geometry of the melt pool [i.e., width ( $W$ ) and height ( $H$ )] of clad was computed and analyzed for the different time period. Figure 19.5 shows the variation of clad width and height with respect to time. As shown in the figure, up to 40 ms, both  $H$  and  $W$  are found to be zero because  $T_{max}$  is less than  $T_{liquidus}$  for this period of time. After 40 ms, both  $H$  and  $W$  gradually increase with time, until initiation of solidification. Note that the solidification is not started from 130 ms, despite laser getting switched off after 130 ms.

From this model, it is observed that the predicted  $H$  and  $W$  start decreasing from 150 ms. In the period from 130 to 150 ms,  $H$  and  $W$  increase in a short range, while the laser is not an active mode because of stagnation of temperature and high thermal conductivity reaches their  $T_{max}$ . From the above figure, it can be concluded that at the given process parameters (Table 19.2), the value of  $W$  is always higher (approximate double) than that of  $H$ , and just after switching off the laser source, it is not necessary that  $H$  and  $W$  suddenly start to decrease.

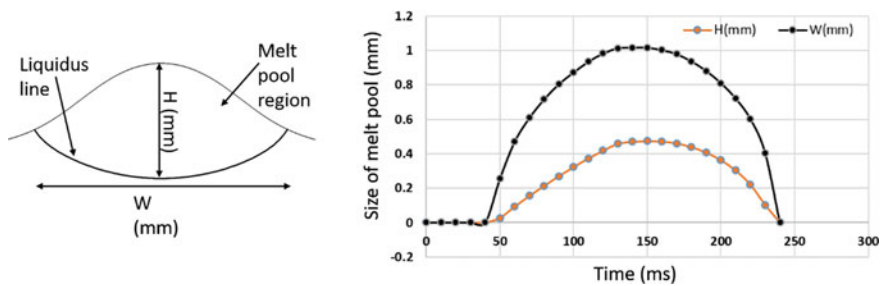


**Fig. 19.5** Variation of melt pool height and width with time

### 19.3.5 Study of Solidification in the Clad Melt Pool

The microstructure formation in the rapid solidification plays a vital role in the surface properties for the various industrial applications. In order to comprehend the rapid solidification processes in the clad melt pool, the solidification parameters such as  $Tt$ ,  $G$ , and  $R$  were analyzed for the prediction of the microstructure. Mathematically,  $R$  can be expressed as  $R = Tt/G$  where  $Tt = dT/dt$  (K/s) and  $G = dT/dx$  or  $dT/dy$  (K/m). Here,  $T$ ,  $t$ ,  $x$ , and  $y$  represent the temperature, time, and coordinates in millimeters, respectively [14]. The chemical composition of alloys and undercooling plays a substantial role in the prediction of microstructure during solidification in the clad melt pool. In this model, to simplify the calculations, the undercooling effect is not considered. Therefore, the solidification parameters are estimated by only heat transfer and fluid flow in the clad melt pool. In this study, the solidification parameters  $Tt$ ,  $G$ , and  $R$  to be calculated in the 14 different locations “a–n” in the clad melt pool are as shown in Fig. 19.6a. Figure 19.6b represents the variation of cooling rate at different positions in the clad melt pool. The value of the magnitude of the ( $Tt$ ) along  $Y$ -axis (at the center of the melt pool) varies with respect to every point. From the above figure, the cooling rate at the central point is lower in comparison with the top and bottom point of the clad melt pool which is well agreed with Gan et al. [15], and variation of magnitude of  $Tt$  is significantly higher along the  $Y$ -direction in comparison with  $X$ -axis (central line). The maximum value of cooling rate is located at the point “n” at the right edge of the melt pool. The magnitude of  $G$  along  $Y$ -direction varies from top to bottom of the clad melt. The value near the top surface

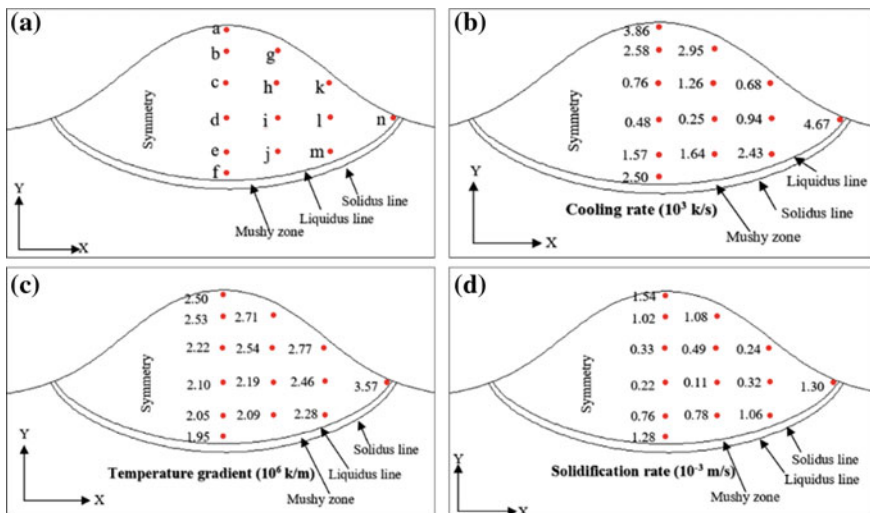


**Fig. 19.6** a Representation of calculation points in the melt pool, b cooling rate, c temperature gradient, and d solidification rate in the clad melt pool

is higher and decreases along the bottom of the surface. The variation of the  $G$  along  $X$ -axis is higher in comparison with the  $Y$ -axis.

As shown in Fig. 19.6c, the solidification rate along the  $Y$ -axis first decreases and then increases from top to bottom of the melt pool. The  $R$  along  $Y$ -direction (in central line) is higher in comparison with  $X$ -direction (central line) because of energy density along  $Y$ -direction is higher with respect to the  $X$ -direction. Therefore, the values of  $G$ ,  $Tt$ , and  $R$  obtained from the above study depict a clear understanding of the thermal map in laser cladding process of Ti alloy. Further, with the help of these values, the state of microstructure evolution can be predicted, as with time, the  $G$  will decrease, and the  $R$  increases leading to sharp drop in  $G/R$  value which ultimately dictates the transition of columnar to equiaxed microstructures in the solidified zone. The developed thermos-fluidic model can be employed as the initial condition for the microstructure prediction model.

## 19.4 Conclusions

A 2D finite element model (FEM) is developed to simulate the heat transfer and fluid flow in the cladding process of the Ti6Al4V alloy. The following conclusions have been drawn from the developed model. The fluid flow in the clad melt is predominantly governed by Marangoni convection, while the thermal buoyancy force plays a minor role. Heat transfer through conduction mode is dominant only in the initial stage of the melt pool, while the heat transfer through advection mode is dominant in the later stages. The maximum value of temperature ( $T_{\max}$ ) in the melt pool was found to be 2966 K at 130 ms, while the maximum magnitude of velocity was achieved 0.51 m/s at 110 ms. The geometry of the melt pool was successfully evaluated, and it was found that both  $H$  and  $W$  vary in a parabolic nature; further, it has been observed that just after switching off the laser, it is not necessary that height ( $H$ ) and width ( $W$ ) suddenly start to decrease. The proposed thermal model can act as a basis for microstructure prediction tool, as it correctly captures the variation in solidification parameters  $Tt$ ,  $G$ , and  $R$  due to the dominating effect of Marangoni convection. In the future, a coupled model will be developed to predict microstructures simultaneously.

## References

1. Leyens, C., Peters, M.: Titanium and Titanium Alloys: Fundamentals and Applications. Wiley (2003)
2. Hussain, M., Kumar, V., Mandal, V., Singh, P.K., Kumar, P., Das, A.K.: Development of cBN reinforced Ti6Al4V MMCs through laser sintering and process optimization. Mater. Manuf. Process. **32**(14), 1667–1677 (2017)
3. Jiang, P., He, X.L., Li, X.A., Yu, L.G., Wang, H.M.: Wear resistance of a laser surface alloyed Ti–6Al–4V alloy. Surf. Coat. Technol. **130**(1), 24–28 (2000)

4. Gray, J., Luan, B.: Protective coatings on magnesium and its alloys—a critical review. *J. Alloy. Compd.* **336**(1–2), 88–113 (2002)
5. Hussain, M., Mandal, V., Kumar, V., Das, A.K., Ghosh, S.K.: Development of TiN particulates reinforced SS316 based metal matrix composite by direct metal laser sintering technique and its characterization. *Opt. Laser Technol.* **97**, 46–59 (2017)
6. Peyre, P., Aubry, P., Fabbro, R., Neveu, R., Longuet, A.: Analytical and numerical modelling of the direct metal deposition laser process. *J. Phys. D Appl. Phys.* **41**(2), 025403 (2008)
7. Kong, F., Kovacevic, R.: Modeling of heat transfer and fluid flow in the laser multilayered cladding process. *Metall. Mater. Trans. B* **41**(6), 1310–1320 (2010)
8. Bedenko, D.V., Kovalev, O.B., Smurov, I., Zaitsev, A.V.: Numerical simulation of transport phenomena, formation the bead and thermal behavior in application to industrial DMD technology. *Int. J. Heat Mass Transf.* **95**, 902–912 (2016)
9. Kumar, A., Roy, S.: Effect of three-dimensional melt pool convection on process characteristics during laser cladding. *Comput. Mater. Sci.* **46**(2), 495–506 (2009)
10. Gan, Z., Yu, G., He, X., Li, S.: Numerical simulation of thermal behavior and multicomponent mass transfer in direct laser deposition of Co-base alloy on steel. *Int. J. Heat Mass Transf.* **104**, 28–38 (2017)
11. Morville, S., Carin, M., Peyr, P., Gharbi, M., Carron, D., Le Masson, P., Fabbro, R.: 2D longitudinal modeling of heat transfer and fluid flow during multilayered direct laser metal deposition process. *J. Laser Appl.* **24**(3), 032008 (2012)
12. Boivineau, M., Cagran, C., Doytier, D., Eyraud, V., Nadal, M.H., Wilthan, B., Pottlacher, G.: Thermophysical properties of solid and liquid Ti-6Al-4V (TA6V) alloy. *Int. J. Thermophys.* **27**(2), 507–529 (2006)
13. Sharma, S., Mandal, V., Ramakrishna, S.A., Ramkumar, J.: Numerical simulation of melt hydrodynamics induced hole blockage in Quasi-CW fiber laser micro-drilling of TiAl6V4. *J. Mater. Process. Technol.* **262**, 131–148 (2018)
14. Ho, Y.H., Vora, H.D., Dahotre, N.B.: Laser surface modification of AZ31B Mg alloy for biowettability. *J. Biomater. Appl.* **29**(7), 915–928 (2015)
15. Gan, Z., Liu, H., Li, S., He, X., Yu, G.: Modeling of thermal behavior and mass transport in multi-layer laser additive manufacturing of Ni-based alloy on cast iron. *Int. J. Heat Mass Transf.* **111**, 709–722 (2017)